JGR Solid Earth

RESEARCH ARTICLE
10.1029/2021JB023469

Estimation of Vs30 at the EarthScope Transportable Array Stations by Inversion of Low-Frequency Seismic Noise

J. Wang[1,2] **and T. Tanimoto**[1]

[1]Department of Earth Science and Earth Research Institute, University of California, Santa Barbara, CA, USA, [2]Now at the University of Chicago, Chicago, IL, USA

Key Points:

- Inversion of low-frequency seismic noise generated by pressure variations provides estimates of Vs30
- Our results provide Vs30 estimates at 744 TA stations for near-surface structure
- The inversion procedure can be widely applied to seismic stations with collocated pressure data

Supporting Information:

Supporting Information may be found in the online version of this article.

Correspondence to:

J. Wang,
jiongwang@ucsb.edu;
jiongwang@uchicago.edu

Citation:

Wang, J., & Tanimoto, T. (2022). Estimation of Vs30 at the EarthScope transportable array stations by inversion of low-frequency seismic noise. *Journal of Geophysical Research: Solid Earth*, *127*, e2021JB023469. https://doi.org/10.1029/2021JB023469

Received 25 OCT 2021
Accepted 22 MAR 2022

Abstract One of the main sources of seismic noise below 0.05 Hz is the atmospheric pressure variation, especially when surface pressure variations are large. When surface broadband seismic stations are equipped with pressure sensors, there is high coherence between pressure and seismic signals at low frequencies. The amount of ground deformation under surface pressure variations reflects the characteristics of near-surface elastic structure and allows us to estimate near-surface shear-modulus structure using an inversion method. In the inversion method, we have the surface observable $\eta(f) = Sz/Sp$, where f is a frequency between 0.01 and 0.05 Hz, and Sz and Sp are the power spectral densities of vertical seismic data and of surface pressure data. We derive depth sensitivity kernels for $\eta(f)$ with which we invert for elastic moduli of the shallow structure. Between 0.01 and 0.05 Hz, sensitivity kernels typically have peaks at depths within the uppermost 100 m. Based on vertically heterogeneous 1-D structures, we estimate Vs30 at 744 USArray Transportable Array stations. Vs30 is the time-averaged shear-wave velocity from the surface to the 30-m depth. We compare our results with various surficial geology maps. Although Vs30 has high horizontal variability over a short distance on the scale of hundreds of meters, we find correlations between Vs30 and large-scale geological structures, such as mapped units and surficial materials. We find good agreement between estimated Vs30 and mapped Quaternary sediment depths, where stations with thicker underlying sediment tend to have slower Vs30.

Plain Language Summary Elastic structure in the uppermost tens of meters can play a crucial role for estimating seismic hazards; however, such structure information is not easy to obtain. We developed an inversion method utilizing low-frequency seismic noise generated by pressure changes at the surface and estimated near-surface elastic structures at 744 stations. Our results provide useful information for seismic hazard studies at these areas, and demonstrate a new and straightforward procedure for estimating near-surface structure.

1. Introduction

The interaction between the atmosphere and the solid Earth through surface pressure variations can be quantified by analyzing low-frequency seismic data with collocated pressure data, particularly data in the frequency band between 0.01 and 0.05 Hz (e.g., Sorrells, 1971; Tanimoto & Wang, 2018). Sorrells (1971) proposed the theoretical framework where the excitation mechanism is wind-related pressure waves that move along the surface and cause ground deformation recorded by broadband seismic sensors. We examine the propagating plane-wave pressure wave model in details by quantitively analyzing collocated wind data in Tanimoto and Wang (2021), and find that the assumption is reasonable when pressure variations are large. Similar principles are also applicable in ocean-bottom-seismometers compliance studies (Crawford et al., 1991) and in evaluating near-surface structure on Mars (Kenda et al., 2017). Expanding on the work of Sorrells (1971), we can use the ratios of collocated seismic and pressure data to estimate the subsurface elastic structure at collocated stations. Better understanding of near-surface structure is important for seismic site effects and ground motion prediction studies (e.g., Borcherdt, 1994; Sánchez-Sesma & Crouse, 2015; Trifunac, 2016). The procedure for retrieving half-space structure at fixed frequencies has been demonstrated and applied to estimate half-space structure at 784 USArray Transportable Array (hereafter TA) stations (Wang & Tanimoto, 2020).

Although the half-space approach provides estimates of near-surface structure in a straightforward manner, it lacks depth constraints that are essential for site effects parameters, such as Vs30. Vs30 is the time-averaged shear-wave velocity from the surface to 30 m below, and it is one of the primary quantities for ground motion prediction studies (e.g., Dobry et al., 2000). In order to estimate Vs30 for a layered structure beneath a station, we

developed an inversion approach by inverting data between 0.01 and 0.05 Hz (hereafter referred to as "the inversion method"; Tanimoto & Wang, 2019). Near-surface elastic structures estimated from the inversion method have been corroborated by comparing with measured Vs30 (Yong et al., 2013) at collocated stations within the Piñon Flat Observatory (Tanimoto & Wang, 2020).

There are other approaches to infer the near-surface structure. These include invasive field-methods such as drilling and sonic logging, noninvasive field-methods such as Multichannel Analysis of Surface Waves (MASW; B. C. Park et al., 1999) with geophone arrays, analysis of the particle motions of body waves (S. Park & Ishii, 2018), and unique deployments such as fiber-optic distributed acoustic sensing (e.g., Dou et al., 2017). Due to the scarcity of Vs30 profiles around the world, it is also common to infer Vs30 using large-scale proxies such as geology maps and topographic slopes (e.g., S. Park & Elrick, 1998; Wald & Allen, 2007). Other shallow-structure techniques such as H/V spectral ratios (HVSR, e.g., Nakamura, 1989) and similarly ZH ratios (e.g., Tanimoto & Rivera, 2008) typically resolve structures at depths measured in kilometers, which are not directly applicable for estimating Vs30. The inversion method presented here can be an addition to the field of seismic hazard studies.

We use the inversion method to estimate the layered structure and Vs30 at 744 TA stations. Our Vs30 results show good agreements with various large-scale surficial geology maps such as Quaternary sediment depths. We also find high degree of similarity between Vs30 and our previously estimated half-space Vs at 0.02 Hz (Wang & Tanimoto, 2020) after comparing results between the layered model and the half-space model. Although the inversion method provides depth constraint and an ability to estimate Vs30, the half-space approach (Tanimoto & Wang, 2018) is still useful because it is more straightforward to adopt and much less computationally expensive, while still gives robust estimates of near-surface structure comparable to Vs30 at certain frequencies.

We present the method and results in the following order; first we present our data with explanations of the quality-control criteria. Second, we describe our inversion method, with examples from two TA stations, 355A and I05D. Lastly, we present Vs30 results at 744 TA stations and compare our results with multiple geological maps.

2. Background

Here we briefly summarize the background of the low-frequency seismic deformation generated by atmospheric pressure changes. Please note that detailed theory and mathematical derivations have been laid out in Tanimoto and Wang (2018, 2019, 2021).

The low-frequency (0.01–0.05 Hz) seismic noise is often associated with surface pressure changes, particularly with a widely adopted excitation model proposed by Sorrells (1971). In the model, the source is propagating pressure wave, where the pressure wave is primarily associated with surface winds. Tanimoto and Wang (2021) points out that when collocated pressure and wind data are analyzed, there is a good correlation between low-frequency pressure data and wind-speed data, especially when wind speeds are fast. Meanwhile when wind speeds are fast, wind directions are generally stable and unidirectional. The correlation between pressure waves and wind flows is consistent with the propagating pressure source in the model. Subsequently, there is high coherence between seismic data and pressure data at low frequencies when pressure variations are large. Figure 1 demonstrates the coherence between vertical seismic data and pressure data between 0 and 0.3 Hz when pressure variations are large. There is a distinct peak in coherence values between 0.01 and 0.05 Hz, which illustrates the correlation between low-frequency seismic and pressure data. When analyzing collocated pressure and seismic data, it is crucial to focus on time intervals with large pressure variations and high coherence, therefore significant seismic deformation; otherwise, poor correlation might be observed, and incorrect conclusions might be reached. Above 0.05 Hz, primary and secondary microseism from the ocean becomes the dominant source for seismic noise.

Interestingly, besides the broad coherence peak between 0.01 and 0.05 Hz, there is another peak below 0.01 Hz in Figure 1. In fact, at lower frequencies, there is another excitation mechanism of seismic noise, where gravity effects become more dominant, namely the effect of gravitational attraction on the sensor mass from the atmospheric density perturbation (e.g., Beauduin et al., 1996; Müller & Zürn, 1983). This physical mechanism of excitation is different from the wind-related pressure waves discussed in this paper. Differences between the two mechanisms are explored in terms of phase differences and formulations in Tanimoto and Li (2020).

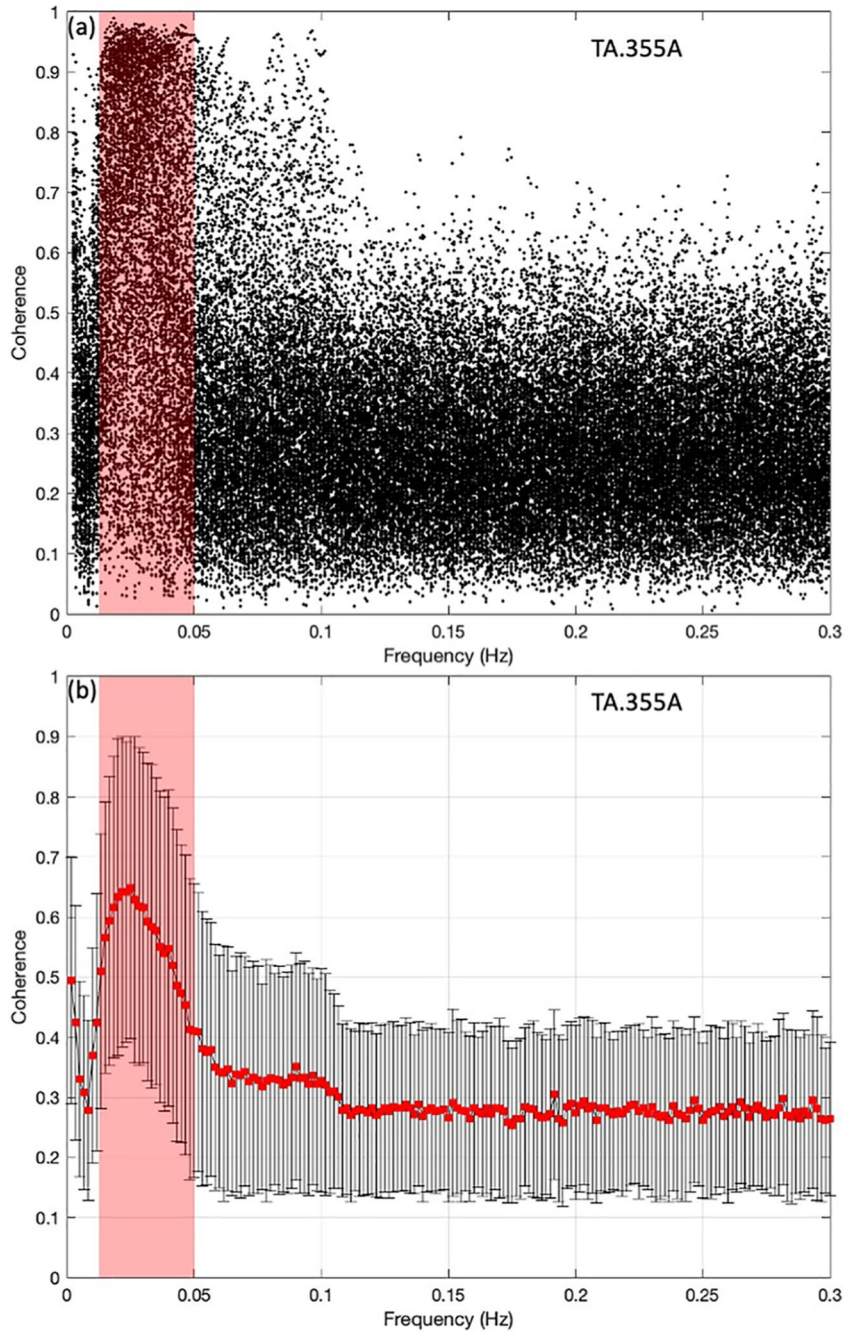

Figure 1. (a). Coherence values between vertical seismic and pressure data at TA station 355A, during days 1–90 of 2012. Shaded area highlights high-coherence frequency bands. (b). Mean coherence values with one standard deviation at 355A during days 1–90. Shaded area highlights high-coherence frequency bands.

Although seismic noise is typically associated with surface pressure variations at low frequencies, it has been widely observed that horizontal seismic data often have much higher amplitudes than vertical seismic data due to the ground tilt (Rodgers, 1968). Meanwhile, the "tilt-contaminated" horizontal signal is a function of the elastic response of the solid Earth, therefore it can still be used for both estimating half-space near-surface elastic structures and constructing layered models. Raspet et al. (2022) recently points out the importance of depth-dependent tilt correction using a homogeneous half-space model; in this model, tilt effects in seismograms rapidly decrease with depth as exp(-ωd/c) where ω is an angular frequency, d is the depth of seismic sensor and c is wind speed.

Relative size of tilt effects between the sensor at depth d to the sensor at the surface is given by this exponential term. For all TA stations in our analysis, depths of sensors are typically around 1–2 m. Because we focus on high-pressure time intervals, wind speed is generally high and typical high-end of wind-speed values is about c = 5 (m/s). Then this exponential term becomes 0.975 at 0.01 Hz and is 0.951 at 0.02 Hz, meaning that we do not see significant correction needed in tilt effects. Similar conclusion is made in Raspet et al. (2022) that such corrections are not necessary for near-surface measurements, which is the case for our studies.

3. Data Analysis

3.1. Data Preprocessing

The dataset comes from the TA stations for which high-quality pressure sensors were added since mid-2011 (Tytell et al., 2016). Broadband seismic stations typically do not have collocated pressure sensors. The lack of collocated seismic and pressure stations is partially the reason for a rather poor quantitative understanding of the land-atmosphere interaction despite early work on the topic (Sorrells, 1971; Sorrells et al., 1971). With the availability of hundreds of collocated TA stations, we now have an unprecedented amount of collocated data to study this phenomenon. Here, we analyze data at TA stations from 1 January 2012 to 1 January 2019. We analyzed 912 stations which cover most of the eastern US and Alaska. For each station, we use three surface seismic channels and one infrasound-sensor pressure channel. We used channels that had a sampling rate of 1.0 Hz. All seismic and pressure data are downloaded from the Incorporated Research Institutions for Seismology Data Management Center (IRIS DMC).

Each TA station typically operated for about 2 years with some backbone stations remained operational for longer periods. We analyze data for the entire duration of each station. We apply standard processing steps on raw time series to compute hourly power spectral densities (PSDs). The processing steps are similar to conventional procedure on analyzing seismic noise, for example, McNamara and Buland (2004). For each one-hour time series, we detrend, apply a Hanning window, compute Fourier spectra, and then remove instrument response (for ground velocity) in the frequency domain. Next, we compute PSDs for seismic and pressure data at frequencies from 0.01 to 0.05 Hz at an increment of 0.005 Hz. We compute hourly coherence between each individual seismic component with pressure. Coherence can be used as an effective indicator of time intervals when the ground is directly deforming due to surface pressure changes (Tanimoto & Wang, 2018). When coherence is high and pressure change is large, the coupling between the atmospheric pressure and the solid Earth is typically strong.

For each hour at each station, we obtain PSDs for three seismic components and the infrasound pressure component. We also compute seismic-pressure coherence for three pairs (each seismic component and the pressure as one pair). For each hour, there are seven quantities estimated at nine discrete frequencies from 0.01 to 0.05 Hz at a frequency interval of 0.005 Hz.

3.2. Half-Space Structure

To prepare for the inversion method, we compute pressure-wave speed, c, and half-space modified shear-modulus, μ, which are used for the construction of starting models. We start the process with some data-culling steps to exclude time intervals when pressure and seismic data are badly correlated. Specifically, we include hourly horizontal PSDs when coherence between two horizontal seismic components and pressure are both higher than 0.7; we include hourly vertical seismic PSDs when coherence between the vertical seismic component and pressure, and coherence between one horizontal seismic component and pressure, are both higher than 0.7. We also impose a pressure threshold at 1 Pa^2/Hz, that is, we only include time intervals when hourly pressure PSDs are higher than 1 Pa^2/Hz. Time intervals with large pressure variations tend to have stronger interaction between the pressure and ground. These coherence and pressure criteria are consistent with our previous practice in Wang and Tanimoto (2020). To better ensure the robustness of our analysis, we apply a 20% trimmed mean method (e.g., Wilcox, 2012) to exclude outliers. By definition, we exclude 20% of both ends of sorted coherent PSDs. The 20% trimmed mean method is shown to be appropriate and effective on excluding significant outliers that could have led to erroneous results (Wang & Tanimoto, 2020).

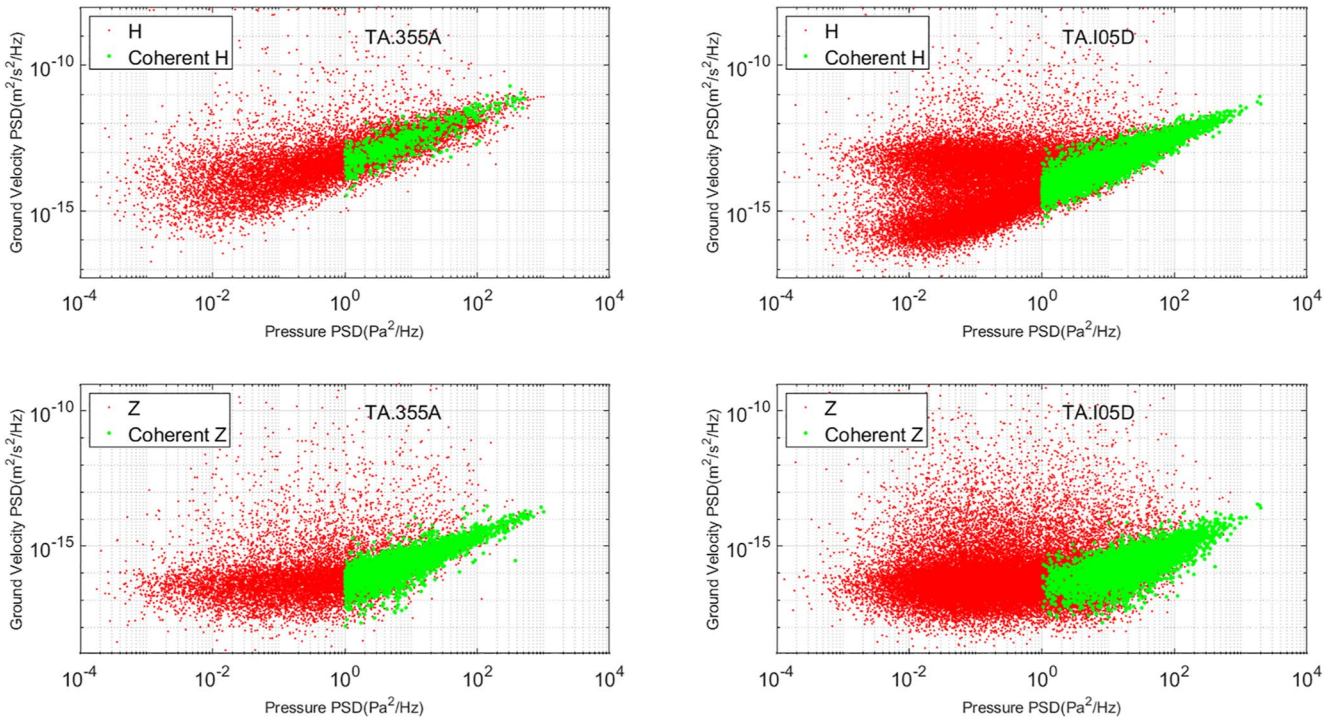

Figure 2. PSD plots of ground velocity vs pressure at 0.02 Hz for TA stations, 355A and I05D. Top panels show horizontal components; bottom panels show vertical components. Each point is an hourly PSD. Time intervals that are coherent with high pressure PSD are highlighted in green.

$$\frac{S_H(f)}{S_P(f)} = \frac{g^2}{4\mu^2\omega^2}\left(\frac{\lambda+2\mu}{\lambda+\mu}\right)^2 \tag{1}$$

$$\frac{S_z(f)}{S_P(f)} = \frac{c^2}{4\mu^2}\left(\frac{\lambda+2\mu}{\lambda+\mu}\right)^2 \tag{2}$$

$$\bar{\mu} = \mu\frac{\lambda+\mu}{\lambda+2\mu} \tag{3}$$

With coherent PSDs of pressure and seismic data, pressure-wave speed and half-space structure can be calculated following Tanimoto and Wang (2018). On the left-hand side of Equations 1 and 2, f is frequency; $S_H(f)$ is PSD of horizontal seismic data, which is the sum of two horizontal seismic PSDs; $S_Z(f)$ is PSD of vertical seismic data; $S_P(f)$ is PSD of pressure data. On the right-hand side of Equations 1 and 2, g is gravitational acceleration; μ is shear-modulus; ω is angular frequency; λ is Lame's parameter; c is pressure-wave speed at the surface. We introduce an alternative quantity $\bar{\mu}$ in Equation 3, which we name "modified shear-modulus".

From Equations 1–3, we can calculate frequency-dependent pressure-wave speed and modified shear-modulus using hourly PSDs and coherence. These will be used in the inversion method to determine the layered structure from which we can get Vs30.

3.3. Quality Control for the Inversion Method

As examples of our analysis, we show results from two stations: 355A and I05D. 355A is a TA station located near Pearson, GA. I05D is a TA station located near Terrebonne, OR. We analyze 21 months of data for 355A and 62 months of data for I05D. Figure 2 is pressure-seismic plots for 355A and I05D. I05D plots have more data points due to its longer duration. As illustrated in Figure 2, if we focus on green points, which are time intervals that pass coherence criterion and pressure threshold, there is clear correlation between pressure PSDs and seismic

Table 1
Data for 355A From 0.01 to 0.05 Hz

Frq (Hz)	kz	kh	ZP_ratio	ΔZP_ratio	HP_ratio	ΔHP_ratio	c (m/s)	Δc (m/s)	μ (Pa)	Δ μ (Pa)
0.010	517	183	1.23E−17	5.54E−18	9.25E−14	3.82E−14	1.80E+00	5.50E−01	2.56E+08	5.30E+07
0.015	2,208	489	1.99E−17	6.54E−18	5.56E−14	1.70E−14	1.97E+00	4.42E−01	2.20E+08	3.37E+07
0.020	3,144	708	2.94E−17	9.53E−18	3.28E−14	9.16E−15	2.34E+00	5.00E−01	2.15E+08	3.01E+07
0.025	3,369	812	4.00E−17	1.12E−17	2.26E−14	5.49E−15	2.62E+00	4.86E−01	2.07E+08	2.51E+07
0.030	2,991	788	5.23E−17	1.57E−17	1.60E−14	4.08E−15	2.97E+00	5.86E−01	2.06E+08	2.62E+07
0.035	2,641	819	6.44E−17	1.90E−17	1.22E−14	3.00E−15	3.24E+00	6.24E−01	2.02E+08	2.49E+07
0.040	2,215	742	7.59E−17	2.65E−17	9.44E−15	2.15E−15	3.50E+00	7.28E−01	2.01E+08	2.29E+07
0.045	1,739	667	9.21E−17	2.93E−17	7.58E−15	1.66E−15	3.82E+00	7.38E−01	1.99E+08	2.18E+07
0.050	1,134	519	1.23E−16	4.54E−17	6.50E−15	1.73E−15	4.30E+00	9.76E−01	1.93E+08	2.57E+07

Note. frq is each discrete frequency, kz is the number of vertical seismic PSDs that pass criteria, kh is the number of horizontal seismic PSDs that pass criteria, ZP_ratio is averaged ratio of S_Z/S_P, ΔZP_ratio is one standard deviation of ZP_ratio, HP_ratio is averaged ratio of S_H/S_P, ΔHP_ratio is one standard deviation of HP_ratio, c is pressure wave speed, Δc is one standard deviation of c, μ is modified shear-modulus, Δ μ is one standard deviation of modified shear-modulus.

PSDs. Simply put, larger surface pressure variations lead to larger ground deformation, which is intuitive for the land-atmosphere interaction. Amplitudes of horizontal PSDs are much larger than amplitudes of vertical PSDs in Figure 2, because low-frequency horizontal seismic signals are dominated by tilt effects (Rodgers, 1968).

Tables 1 and 2 show summarized results for 355A and I05D. We create a data table for every TA station. We use the information in the table to determine whether a station is a good candidate for the inversion. We construct starting models for the inversion based on pressure-wave speed c and modified shear-modulus μ at discrete frequencies.

"kh" and "kz" fields in Tables 1 and 2 are numbers of one-hour coherent and high-pressure time intervals for the entire duration of two stations for both horizontal and vertical components. The remaining columns are computed using Equations 1–3 with a 20% trimmed mean approach (e.g., Wilcox, 2012). Standard deviations are estimated from the distribution of coherent data segments (see green points in Figure 2). 355A and I05D both have large kh and kz, as illustrated in Figure 2. However, there are TA stations that have low kh and kz, which suggest very few time intervals have high seismic-pressure coherence. The lack of coherent time intervals at some stations is potentially related to environmental factors such as local microclimates or unique site conditions, where hard-rock sites may have little deformation under surface pressure changes (Wang & Tanimoto, 2020).

To ensure the robustness of the inversion, we impose two quality-control steps on all TA stations. First, a station will be included in the analysis only if it has five or more frequencies with both kh and kz larger than 10. With

Table 2
Data for I05D from 0.01 to 0.04 Hz.

Frq (Hz)	kz	kh	ZP_ratio	ΔZP_ratio	HP_ratio	ΔHP_ratio	c (m/s)	Δc (m/s)	μ (Pa)	Δ μ (Pa)
0.010	682	4,294	5.09E−18	2.80E−18	1.09E−14	2.81E−15	3.37E+00	1.02E+00	7.47E+08	9.61E+07
0.015	2,893	4,707	7.68E−18	2.96E−18	6.11E−15	1.45E−15	3.69E+00	8.34E−01	6.65E+08	7.87E+07
0.020	3,988	4,975	1.01E−17	4.24E−18	3.97E−15	1.02E−15	3.94E+00	9.65E−01	6.19E+08	7.91E+07
0.025	4,369	5,343	1.21E−17	4.56E−18	2.79E−15	6.53E−16	4.11E+00	9.11E−01	5.90E+08	6.90E+07
0.030	4,236	5,257	1.36E−17	5.41E−18	2.05E−15	5.08E−16	4.23E+00	9.92E−01	5.74E+08	7.09E+07
0.035	3,782	5,198	1.59E−17	5.88E−18	1.59E−15	3.70E−16	4.46E+00	9.70E−01	5.58E+08	6.47E+07
0.040	3,151	4,717	1.77E−17	7.13E−18	1.26E−15	2.96E−16	4.62E+00	1.08E+00	5.49E+08	6.44E+07

Note. All fields are the same as Table 1.

this constraint the number of stations was reduced to 754 from 912. Second, if a station is qualified by the first step, only those frequencies for which kh and kz are greater than 10 are included in the inversion. For example, if a station has large kh and kz from 0.01 to 0.04 Hz, but not at 0.045 and 0.05 Hz, we will invert the structure to fit data only from 0.01 to 0.04 Hz. We run the inversion algorithm at 754 qualified stations and eventually obtain stable results at 744 stations.

4. Inversion Method and Examples

Here we briefly summarize steps in the inversion method to provide context for the rest of the paper. More detailed background theory and inversion procedure can be found in the Supporting Information S1 and Tanimoto and Wang (2019). In the inversion method, the fundamental idea is to construct a starting model (layered structure), perturb and update this model to fit data at multiple frequencies from 0.01 to 0.05 Hz. Specifically, we aim to fit surface observable η(f), which we define as the following.

$$\boldsymbol{\eta}(\mathbf{f}) = \frac{\mathbf{S_Z}(\mathbf{f})}{\mathbf{S_P}(\mathbf{f})} \tag{4}$$

$\eta(\mathrm{f})$ is the ratio between vertical seismic and pressure PSDs at discrete frequencies; it is "ZP_ratio" in Tables 1 and 2. Pressure-wave speed can be estimated using Equations 1 and 2, and it is typically around 1–10 m/s, as shown in Tables 1 and 2. Notably, pressure-wave speed is much slower than seismic waves; this leads to the sensitivity at much shallower depths compared to traditional seismic methods at these low frequencies. $\eta(\mathrm{f})$ is frequency-dependent; fitting of $\eta(\mathrm{f})$ will provide constraints on the layered model.

Throughout this method section, we present examples of the inversion at TA stations 355A and I05D. Data from these two stations are illustrated in Figure 2; important values are tabulated in Tables 1 and 2.

4.1. Inversion Method

We first construct starting models for each TA station by using half-space structure at different frequencies. Half-space structures are calculated following Equations 1–3. From sensitivity kernels for $\eta(\mathrm{f})$ with respect to shear-modulus, we find a crude empirical relationship between pressure-wave speed and peak-depth of kernels at different frequencies.

$$\mathbf{H}(\mathbf{f}) \cong \frac{0.15 * \boldsymbol{c}(\mathbf{f})}{\mathbf{f}} \tag{5}$$

where H(f) is the peak depth of the shear-modulus kernel, c(f) is the pressure-wave speed and f is the frequency. We typically selected from 0.01 to 0.05 Hz but the exact range varied depending on the quality of data. After obtaining peak depths at each discrete frequency, we align the half-space elastic structure to the corresponding peak depths. We interpolate parameters between fixed peak depths from these discrete frequencies. For example, a station with pressure-wave speed of 5 m/s at 0.01 Hz will have its deepest H(f) at 75 m (Equation 5). Then we assign density, Vp and Vs converted from modified shear-modulus at 0.01 Hz to the depth of 75 m in the starting model. The conversion follows the model BJ97gr760 (Boore, 2016), which provides combinations of density and seismic velocities. We match modified shear-modulus to a set of density and seismic velocities in the model BJ97gr760. Vs profiles shown as dashed lines in Figure 3 are starting models of 355A and I05D based on information from Tables 1 and 2.

In practice, this design of starting models works quite well with structures found by the inversion converging to the quantity $\eta(\mathrm{f})$ quickly.

After setting up vertically heterogeneous starting models, we apply the inversion method following Tanimoto and Wang (2019). In practice, we perturb and update layered models in each iterative step to fit the target quantity $\eta(\mathrm{f})$. Sensitivity kernels (Figure 4) are computed for each updated model and used to solve for perturbations of shear-modulus and bulk modulus. These perturbations are used to update the layered model.

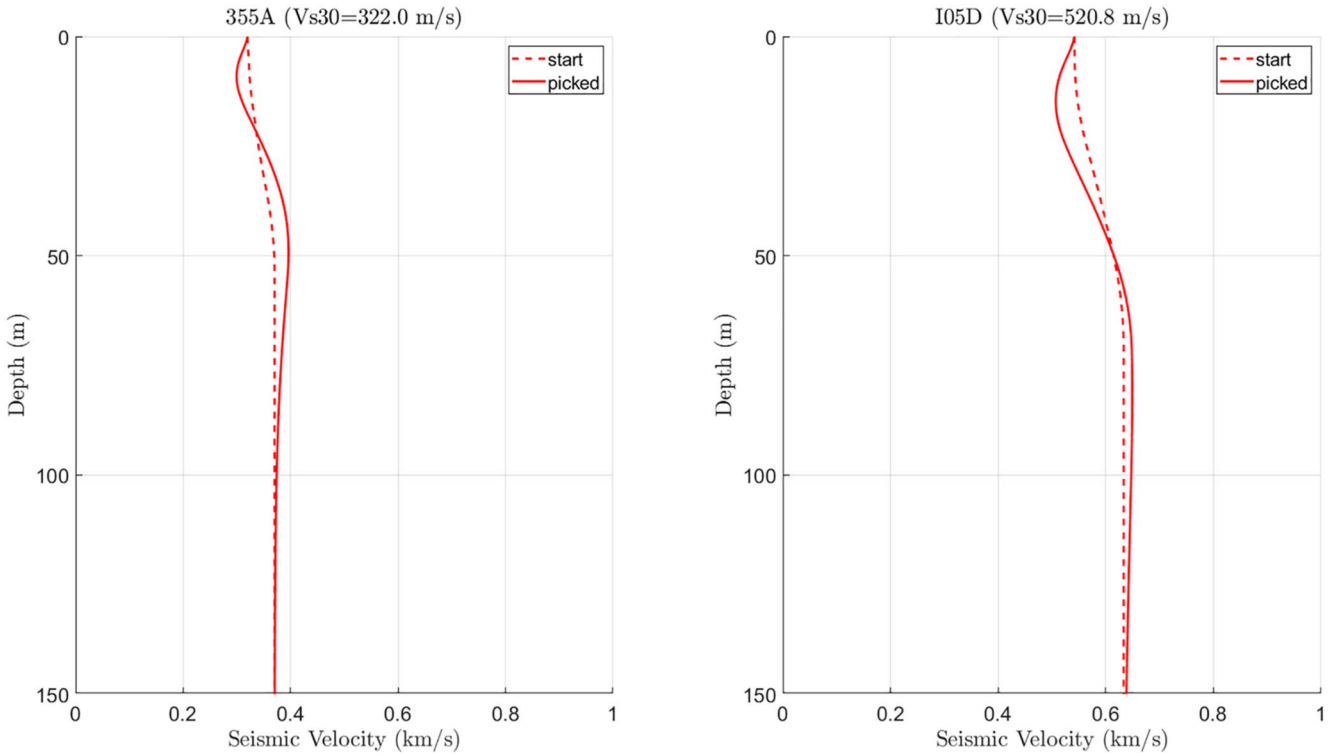

Figure 3. Starting and final Vs models at 355A and I05D.

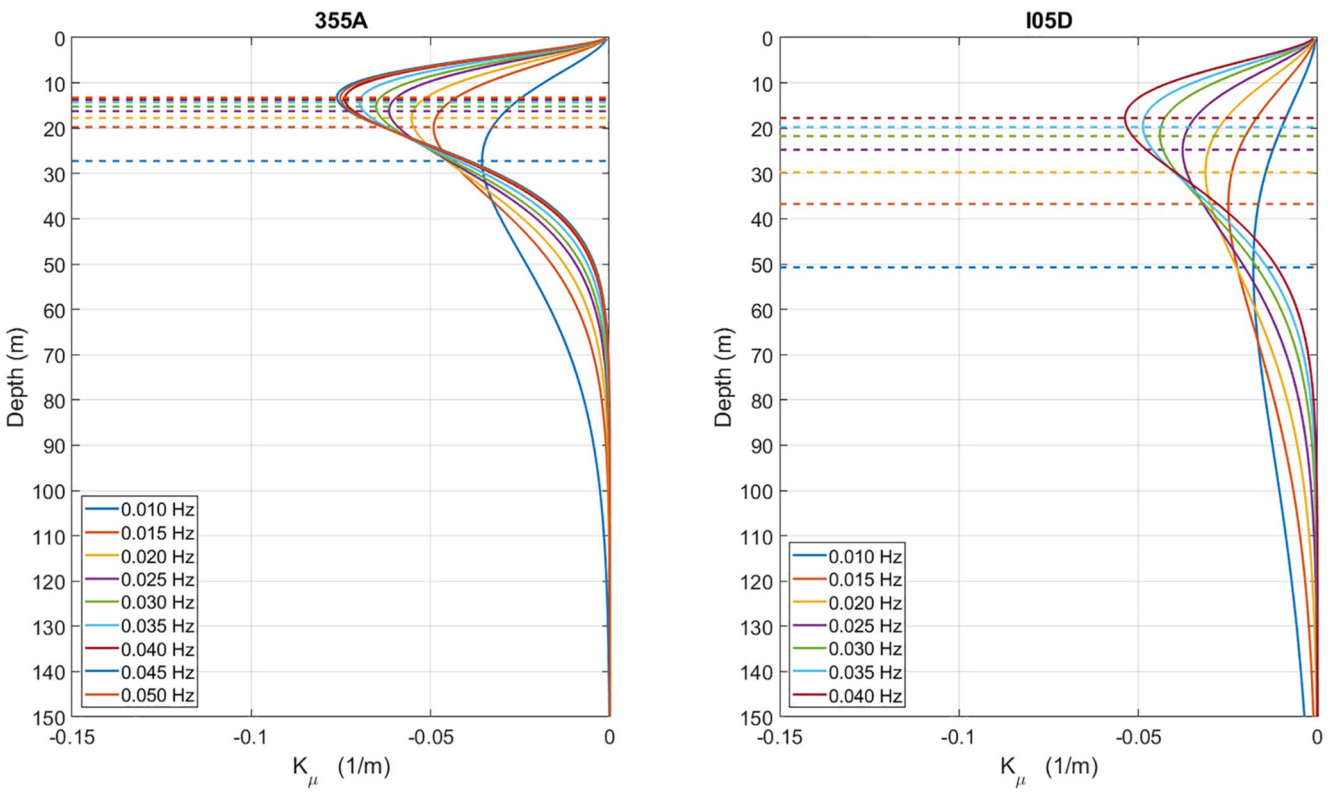

Figure 4. Sensitivity kernels of shear-modulus. Dashed lines demonstrate peak depths at all frequencies.

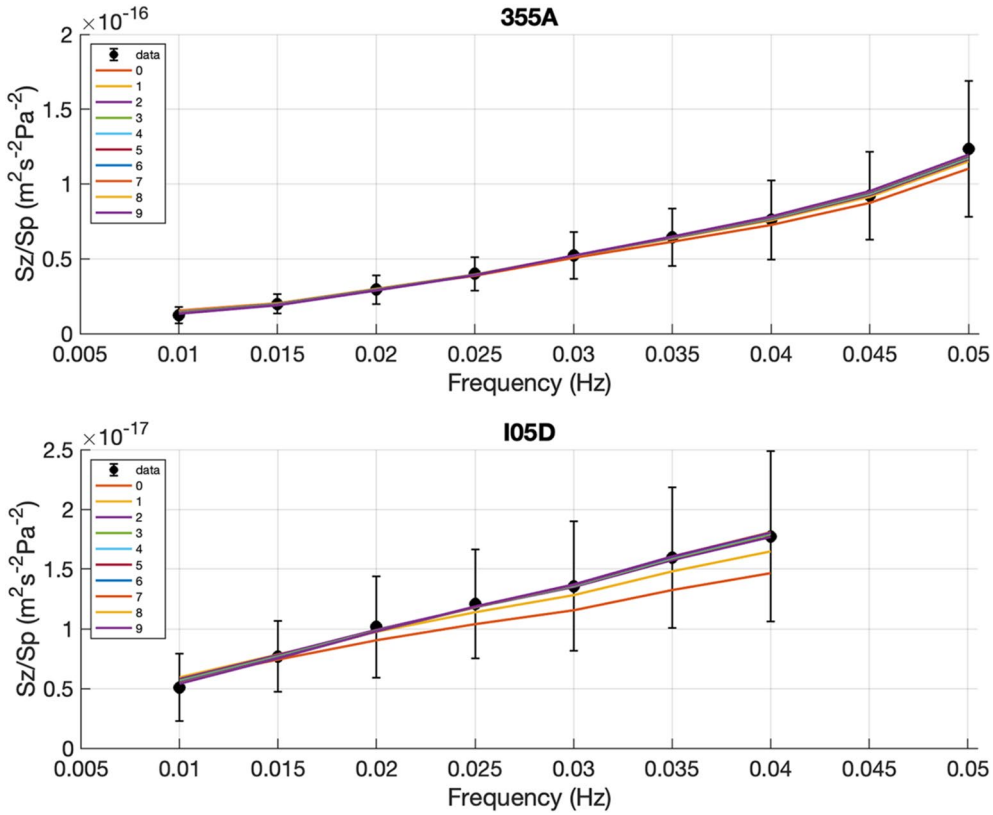

Figure 5. Nine inversion iterations and model fit at 355A and I05D. Data are observed $\eta(f)$ with error bar as $\pm 1\sigma$. Nine lines are theoretical $\eta(f)$ computed from layered models at each iteration.

4.2. Model Fit and Variance Reduction

With the inversion framework set up, we can start the numerical processing. In practice, at each TA station, we iterate the inversion nine times although an optimal model is typically found at earlier steps.

In Figure 5, we illustrate a theoretical $\eta(f)$ computed from each layered model with the starting model as the 0-th iteration. Theoretical $\eta(f)$ is compared with observed $\eta(f)$ listed in Tables 1 and 2. For 355A, the starting model fits the data well, whereas the starting model of I05D fits data less well but still within $\pm 1\sigma$ of the data. At both stations, the inversion converges in one or two iterations after which the models remain relatively constant. The upper frequency limit is 0.05 Hz for 355A and is 0.04 Hz for I05D. For all stations, we perform inversion up to 0.05 and 0.04 Hz; then we visually inspect the goodness of fit for both cases. Typically, data near 0.05 Hz show more scatter and uncertainty, presumably because energy from the ocean waves starts to outweigh the effect of atmospheric pressure (e.g., Tanimoto & Wang, 2018). By examining sensitivity kernels (Figure 4) we note that peak depths for 0.04 and 0.05 Hz are very similar. We surmise that the choice on upper frequency limit between 0.04 and 0.05 Hz has minor influence on the resulting layered structure.

After nine iterations, we decide which iteration is the final model by determining the improvement of the misfit using variance in Equation 6 and variance reduction between the consecutive models. In Equation 6, σ^2 is the variance, i is the index for frequencies, from 0.01 to either 0.04 or 0.05 Hz at an interval of 0.005 Hz; therefore m is seven or nine depending on the upper frequency limit. η_o^i is the observed η in each iteration, whereas η_T^i is the theoretical η for a given model.

$$\sigma^2 = \sum_{i=1}^{m} \left(\eta_o^i - \eta_T^i\right)^2 \tag{6}$$

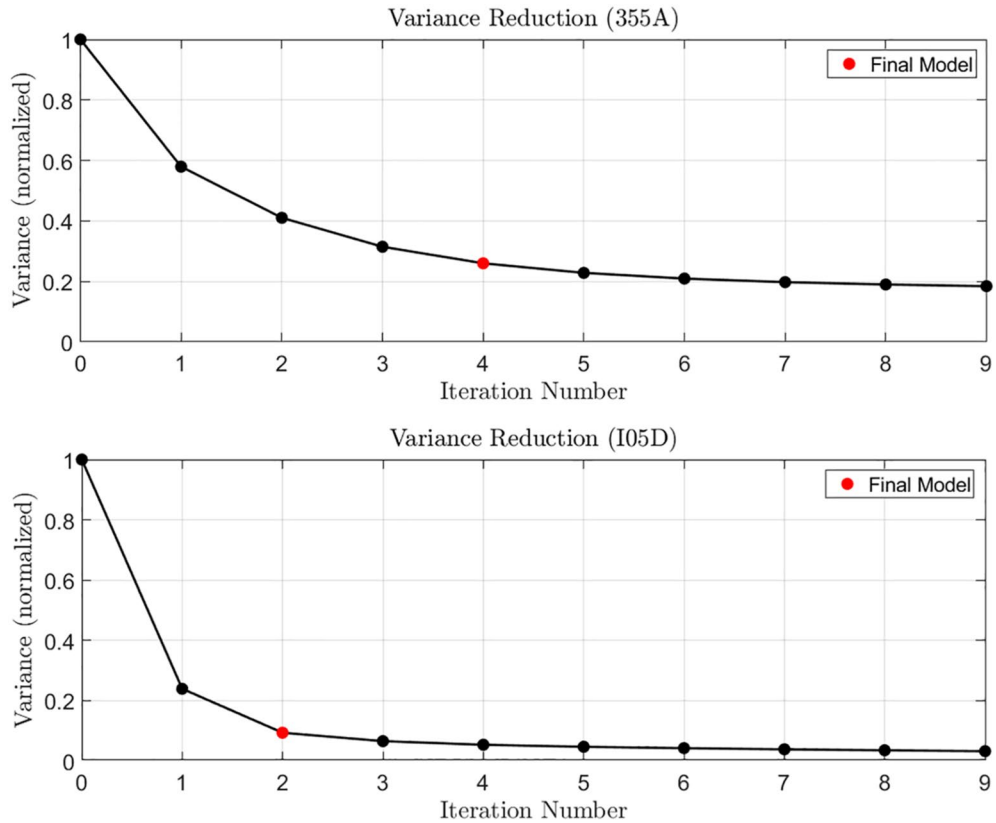

Figure 6. Variance reduction at 355A and I05D. Red points are the final models.

In most cases, the inversion converges after one or two iterations. Although the misfit could be further reduced with more iterations, improvements become quite small. Therefore, we select the final model when the normalized variance reduction of the next iterative model is less than 5% of the previous model.

Figure 6 show variance reduction for both 355A and I05D. All variance values are normalized to the variance of the starting model. In both cases, there are significant improvements of the misfit after the first iteration. Misfits then stay relatively flat for several more iterations which suggest improvements on the goodness of fit become small. For example, at I05D, the normalized variance in the first iteration is 23.9%, that is, a variance reduction of 76.1%. Normalized variance at the second iteration is 9.4%, that is, a variance reduction of 14.5%, still larger than the 5% threshold. Normalized variance at the third iteration is 6.6%, which suggests a variance reduction of only 2.8%, which falls below the 5% threshold. Therefore, for I05D, the final model is the layered model at the second iteration. While the 5% threshold is rather arbitrary, selecting nearby iterations would give similar results as seen from the convergence in Figure 5. After a final model is determined, we can estimate Vs30 from the picked model.

We estimate standard deviations of Vs30 results using covariance matrices of data measurements and model parameters, which are common for least-square inversions (e.g., Tarantola, 2005). Once we obtain standard deviations of shear-modulus and bulk-modulus in layered structures, we can estimate uncertainties in layered Vs and Vs30. Vs30 uncertainties are typically around 20%–30% of the mean Vs30 estimate.

5. Results

5.1. Vs30 at 744 Stations

For all 744 stations, we follow the steps described in Sections 3 and 4. We pick time intervals with high coherence and large pressure, construct individual starting models from half-space models at discrete frequencies, invert for

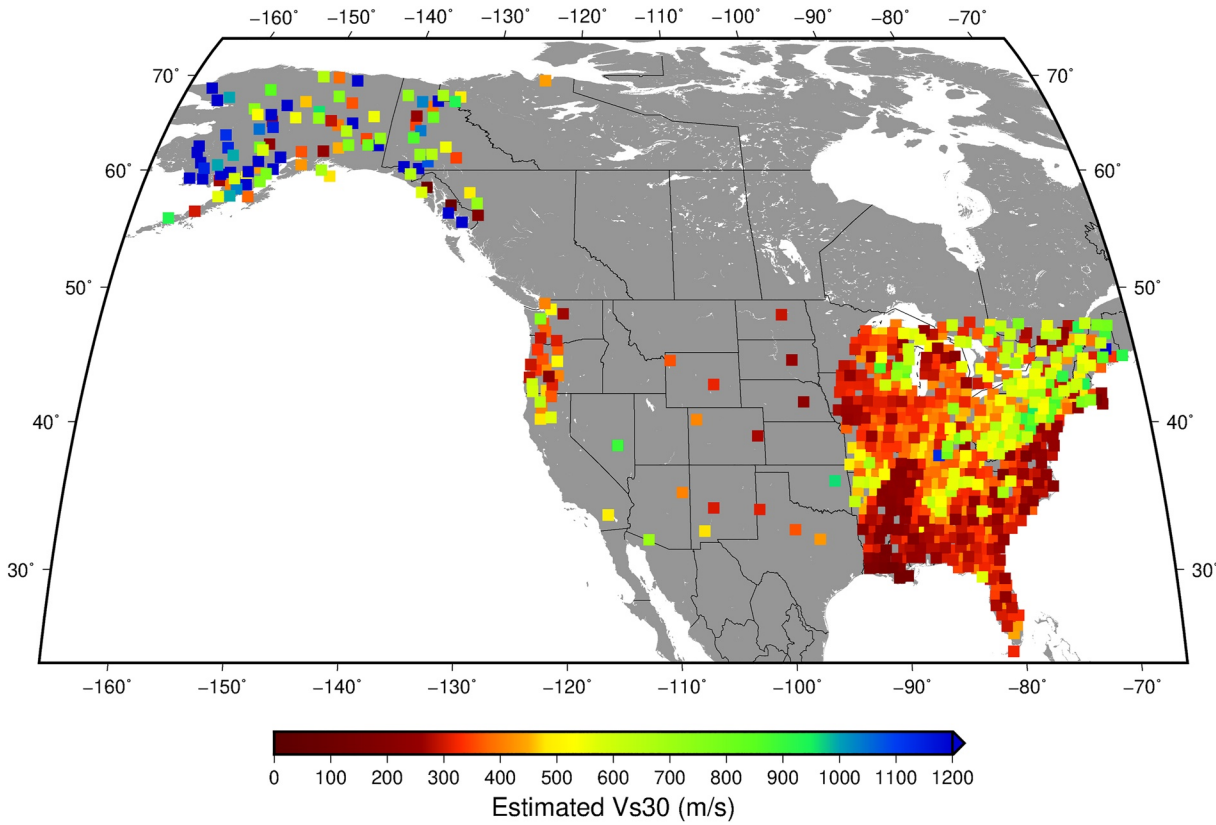

Figure 7. Vs30 results at 744 TA stations. Note that color bar saturates at 1,200 m/s. Each station is located at the center of each square.

layered structures with nine iterative steps, and determine final models by examining variance reduction. Then we estimate Vs30 at these TA stations. Vs30 values for all 744 stations can be found in Supporting Information S2. Vs30 is defined as time-averaged shear-wave velocities in the top 30 m, and can be computed following Boore (2004). Vs30 of 355A and I05D are reported in the titles of Figure 3.

Figure 7 illustrates the spatial distribution of Vs30 values. There are two predominant regions that have distinct Vs30 values among stations in the Eastern United States. First, many stations along the Appalachian region have Vs30 faster than 700 m/s. Second, many stations within the Mississippian Alluvial Plain have Vs30 slower than 300 m/s. Similar patterns can be seen in various Vs30 models (e.g., Thompson & Silva, 2013; Wald & Allen, 2007). These two patterns are consistent with local geological settings. Many TA stations in the high-latitude regions such as Alaska and Territory of Yukon are quite unique. Some of these stations have Vs30 higher than the upper limit of the color bar (1,200 m/s) and often have high uncertainties in the half-space estimates. There is evidence of significant seasonal changes in the low-frequency seismic noise, where amplitudes are much higher in the summer than amplitudes in the winter. This is potentially related to drastic temperature changes in high-latitude regions. Interpretation of these seasonal changes require detailed analysis of meteorological data at individual stations, which is outside the scope of this paper and will be explored in the future.

In Figure 8, we can further examine distributions of Vs30 in the Appalachian and in the Mississippi alluvial plain. The group "All" includes stations in two regional groups. In the stacked histogram (panel a of Figure 8), Appalachian stations (blue) accumulate at faster Vs30 and Mississippi stations (red) accumulate at slower Vs30. Such distributions confirm the visual patterns observed in Figure 7. In panel (d) of Figure 8, a box plot of the same three groups presents similar information as histograms shown above, where each box encompasses stations in their respective histogram. While distributions of the three groups overlap, the median Vs30 among each group is distinct. All contiguous US stations have a median Vs30 of 360 m/s, Appalachian stations have a faster median Vs30 of 544 m/s and Mississippi stations have a slower median Vs30 of 213 m/s. Information shown in the box plot is consistent with visual patterns seen in Figure 7. Besides these large-scale analyses of our results,

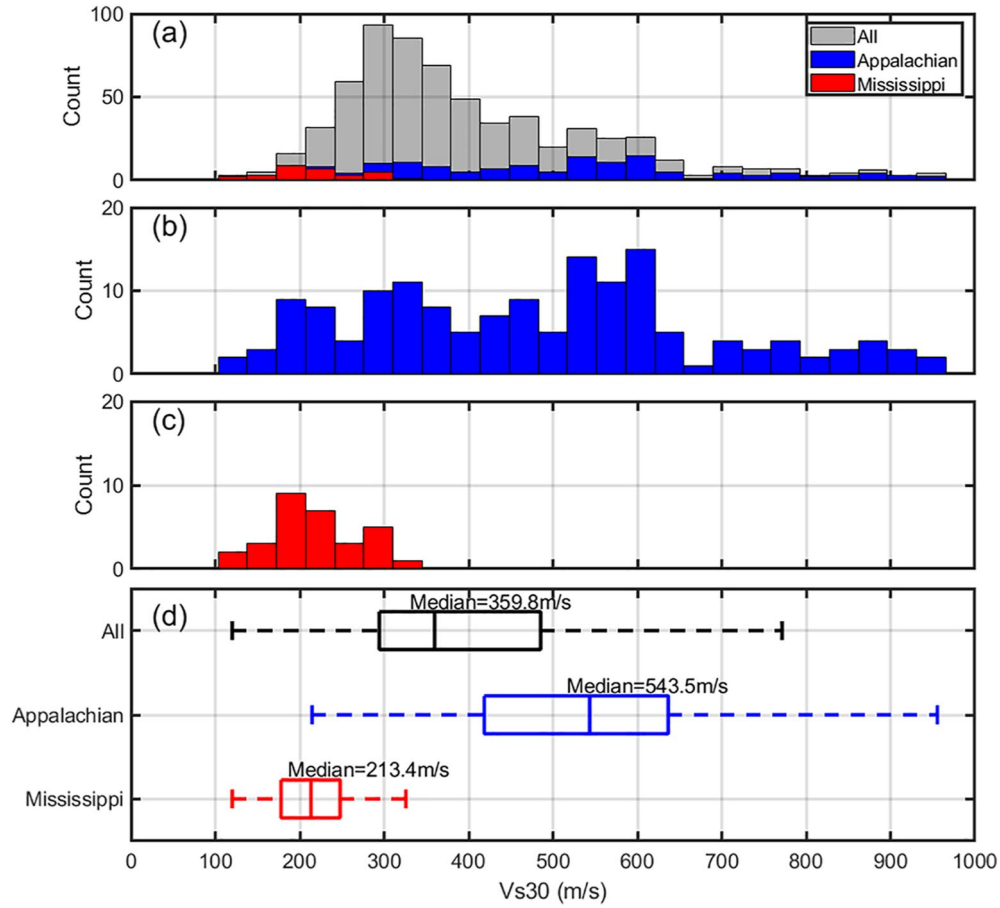

Figure 8. (a) Stacked histogram among three groups: all stations in the contiguous United States, Appalachian stations and Mississippian stations. "All" stations include the latter two groups. (b) Histogram for all "Appalachian" stations. (c): Histogram for all "Mississippi" stations. (d): Box plot for three groups the same as the top panel. Vertical line within each box is the median Vs30 of that group. Boundaries of each box represent 25th and 75th percentile of that group. Whiskers extending to each side represent ±2.7σ of that group. Outliers outside of whiskers are omitted, but observable in the top panel.

we validated results from the inversion by comparing our estimates of Vs30 with measured Vs30 in the Southern California (Tanimoto & Wang, 2020).

5.2. Comparison With Geological Maps

In this section, we compare our Vs30 results with two surficial geology maps. One map covers most of the northeast United States (Soller & Garrity, 2018); it includes sediment depths and overlaps with 215 TA stations. The other covers the conterminous United States (Soller et al., 2012) and includes different interpretations of surficial materials. This map includes 583 TA stations. We also compare our results with the Geologic Map of North America (GMNA; Garrity & Soller, 2009) which is a database of geological units such as rock types and rock ages. When near-surface structure is unknown, large-scale geological information and topographic slopes are commonly incorporated as proxies to infer parameters such as Vs30 (e.g., S. Park & Elrick, 1998; Wald & Allen, 2007). In Wang and Tanimoto (2020), we quantitatively compared our half-space results with the USGS Global Vs30 Mosaic (Wald & Allen, 2007), which is based on topographic slopes. We found that although large-scale patterns are consistent, station-wise correlation with interpolated Vs30 values from the gridded model is poor (see Figure S1 in Supporting Information S1). This is expected because large-scale Vs30 models are not appropriate for interpreting local structures. Similarly here, correlations with large-scale geology maps will also be limited because it is unrealistic to expect accurate information at a local scale, that is, at a single station. In

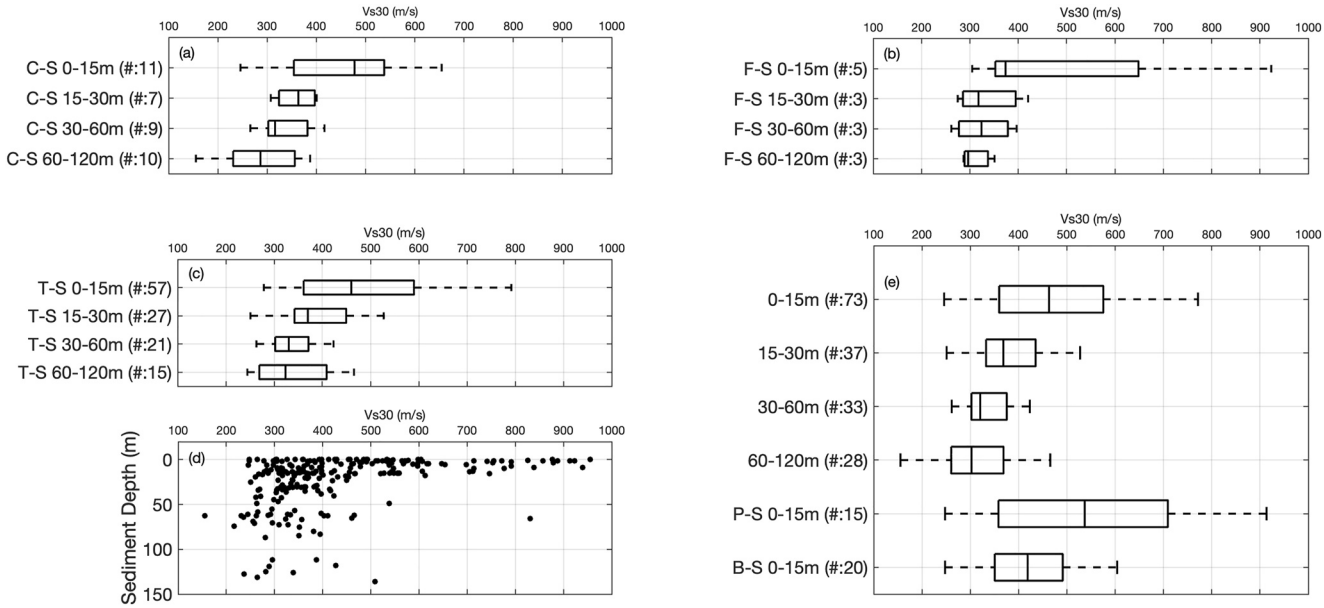

Figure 9. (a)–(c). Box plots of estimated Vs30 (x-axis) with respect to their Quaternary sediment depths. Vertical line within each box is the median Vs30 of that group. Boundaries of each box represent 25th and 75th percentile of that group. Whiskers extending to each side represent $\pm 2.7\sigma$ of that group. (a). "C-S" stands for "coarse-grained sediments" and followed by their depths in meters. Numbers in the bracket are counts of stations within the unit. (b). "F-S" stands for "fine-grained sediments." (c). "T-S" stands for "till sediments." (d). Scatter plot between estimated Vs30 and sediment depths. (e). Box plot of Vs30 with three categories combined at different sediment depths. Top four boxes include all stations from (a) to (c). Bottom two boxes are two unique units. "P-S" stands for "Patchy Sediments." "B-S" stands for "Bedrocks or Sediments.".

this study, we compare with the various geological maps to understand the generality of our results. The goal is to find possible correlations, not to interpret each geology map in-depth.

We group TA stations with defined units on each map by matching stations with defined polygons on maps. We look at distributions of estimated Vs30 within separate units and interpret them based on three categories of information: sediment depth, surficial material, and geological unit.

We first compare estimated Vs30 at 215 TA stations with Quaternary sediment depths compiled in Soller and Garrity (2018). This covers previously glaciated US east of the Rocky Mountains. In panels (a) through (c) of Figure 9, most groups have overlapping distributions of Vs30. However, in all three categories of surficial sediments (coarse-grained, fine-grained and till), there are large differences between groups with sediment depths of 0–15 m and 15–30 m; "coarse-grained" and "fine-grained" sediments are related to wind or water transports. Intuitively, near-surface structure with coarse-grained sediments, such as sands and gravels, should have faster velocities than fine-grained sediments, such as silt and clay, due to their different material properties and depositional environments where coarse-grained sediments are often deposited on steeper slopes. Such interpretations are used in defining site classes based on measured profiles (Wills et al., 2000); however, this correlation often does not hold when inferring Vs30 using large-scale geological maps. Studies commonly demonstrate that locations defined as "coarse-grained sediments" do not have significantly different Vs30 from locations defined as "fine-grained sediments" (e.g., S. Park & Elrick, 1998). At a local scale, limited resolution of large-scale geological maps and uncertainties in the sediment depths likely contribute to the lack of correlations (Will et al., 2015). In our comparisons between these two categories of sediments, median Vs30 of "coarse-grained sediments" are faster than that of "fine-grained sediments" in both "0–15m" and "15–30 m" groups. This is consistent with the interpretations above; however, the number of "fine-grained sediment" stations is small, thus less robust. On the other hand, till is the most widespread unit due to the unique geographic setting of this map. Till sediments are deposited from the interaction with previous glaciers in the region. Till sediment generally have faster velocities than typical soils (Thompson & Silva, 2013). Median Vs30s of "till" stations are similar to that of "coarse-grained sediments" stations, which are both faster than median Vs30 of "fine-grained sediments" stations.

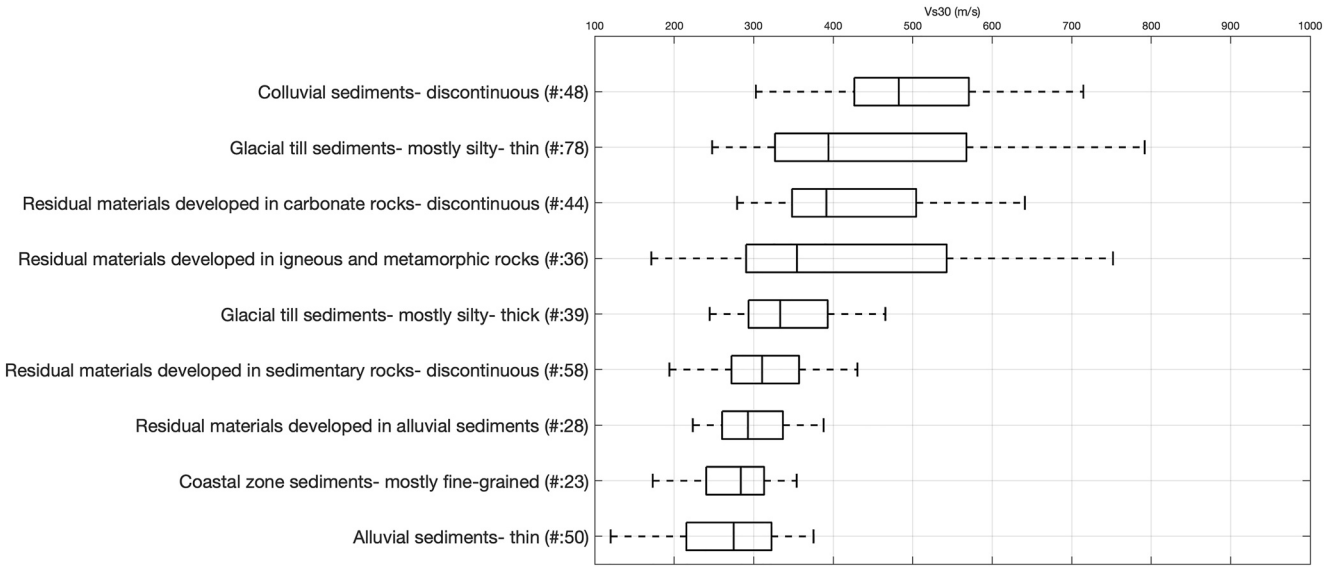

Figure 10. Box plot of estimated Vs30 (x-axis) with respect to their surficial material units. Y-axis tick marks include unit names and the number of stations within that unit. Vertical line within each box is the median Vs30 of that group. Boundaries of each box represent 25th and 75th percentile of that group. Whiskers extending to each side represent $\pm 2.7\sigma$ of that group.

All groups with the thinnest sediments (0–15 m) have wider distributions of Vs30, and their median Vs30s are faster than groups with thicker sediments. Wider distributions suggest Vs30s are more variable within the areas of thin sediments. This should be expected because stations with minimal underlying sediments will have significantly faster Vs30 than stations with 15 m of underlying sediment. "Till sediments" groups in panel (c) include the most stations among a total of 215 stations. We observe a large decrease in median Vs30s from "T-S 0–15 m" to "T-S 15–30 m" and a small decrease from "T-S 15–30 m" to "T-S 30–60 m.f." Distributions of Vs30 between "T-S 30–60 m" and "T-S 60–120 m" are similar. Generally, stations with thicker underlying sediments should have slower Vs because seismic waves travel with slower speeds in the unconsolidated sediments than in bedrocks. Considering Vs30 is an averaged quantity for shear-wave velocities in the shallowest 30 m, we can expect slower Vs30 in areas with thicker sediment depths. Once sediment depths exceed 30 m, the presence of deeper sediments should not affect Vs30. Observations are consistent with this general principle. In panel (e), first four boxes are ensembles of three categories mentioned earlier. Two unique groups in panel (e) are "patchy sediments 0–15 m" and "bedrocks or sediments 0–15 m." While these two groups have faster median Vs30 and wider distributions than groups with thick sediments, one would expect much faster Vs30 if bedrock is exposed at or very close to the surface. Distribution of Vs30 at these locations suggest that some unconsolidated sediments likely exist, which could be due to map uncertainties. Panel (d) of Figure 9 shows a scatter plot of Vs30 results versus sediment depths. Sediment depths are extracted from the raster file provided in Soller and Garrity (2018); this file assigns specific depths at all points. Although there is no distinct correlation, we observe one important pattern similar to three box plots: for stations with thin sediments, Vs30 has a wide range and some stations have fast Vs30, and for stations with tens of meters of sediments or more, Vs30 is slow. This pattern suggests that fast Vs30 stations are located in places with very thin sediments.

The second comparison is between 583 stations and their mapped surficial material units in Soller et al. (2012). This map spans the conterminous United States; it overlaps with more stations than the first comparison. It includes only descriptions of surficial materials but not specific thickness of sediments. Figure 10 includes all groups with more than 20 stations. It shows nine groups of stations that are defined by their surficial materials. These are sorted by their median values of Vs30. Three top groups are defined by "discontinuous" or "thin" sediments, and three bottom groups are defined by "Alluvial" or "Coastal zone" sediments. Top two groups are associated with colluvial and glacial till sediments. Colluvial (loess) and glacial till sediments typically have faster velocities than typical soils (Thompson & Silva, 2013). Meanwhile, alluvial and coastal sediments are expected to have slower seismic velocities. Despite the largely overlapping distributions, groupings of stations (Figure 10) fit our general understanding on the relationship between different types of surficial sediments and near-surface

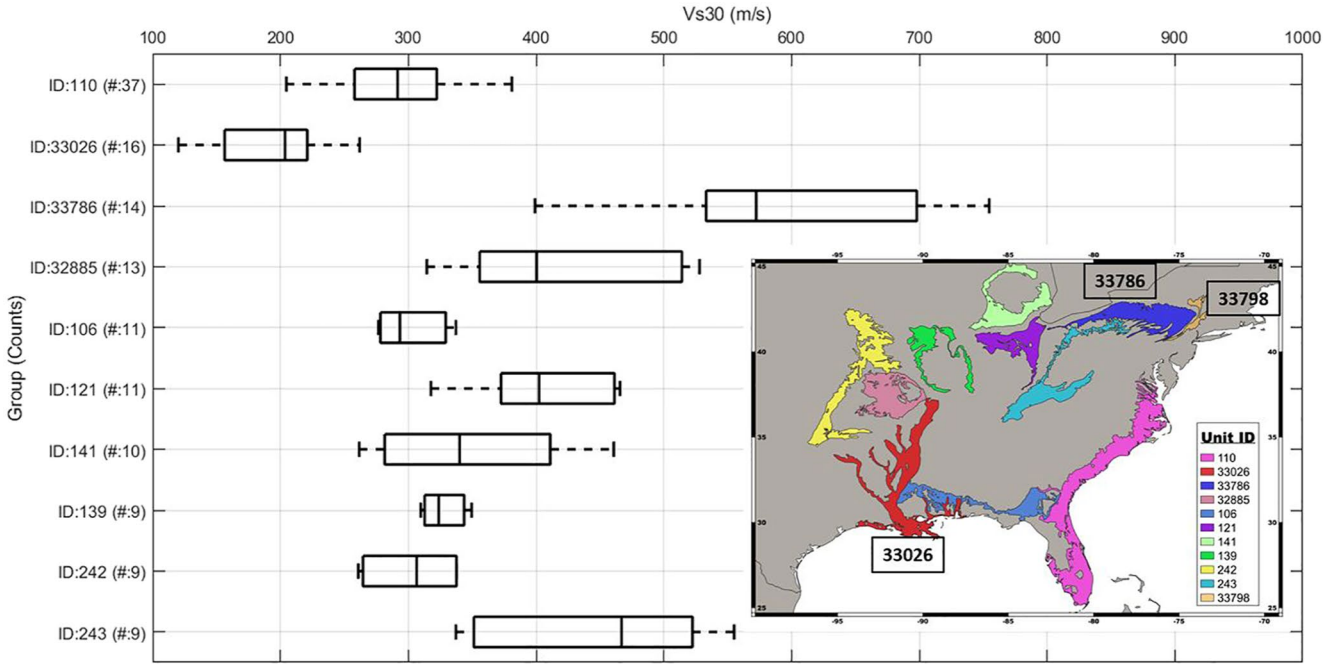

Figure 11. Box plot of estimated Vs30 (x-axis) with respect to their geological unit IDs. Units are highlighted on the onset map. Three focused units are labeled for clarity. Y axis tick marks include unit ID and the number of stations within that unit. Vertical line within each box is the median Vs30 of that group. Boundaries of each box represent 25th and 75th percentile of that group. Whiskers extending to each side represent $\pm 2.7\sigma$ of that group.

velocities. Although there is no information on sediment depths, surficial material interpretations from Soller et al. (2012) are consistent with our Vs30 results.

Geological unit IDs are unique identifier numbers assigned to each unit in the GMNA. These IDs are non-repetitive, meaning geological units will have different IDs if they are at different locations, even if they have the same geological interpretations of rock types and ages. These ID numbers are rather arbitrary and are only related to the order of polygons in the shapefile. Therefore, grouping of stations by unit IDs is indicative of their locations and serves as an index to distinct nearby stations. Figure 11 shows 10 geological units with most stations contained within. There are two units with distinct distributions, unit 33026 and unit 33786. Unit 33026's distribution of Vs30 is much slower than other units shown in the plot. It is described as a Quaternary sedimentary rock unit. As seen on the onset map, unit 33026 covers much of the Mississippi Alluvium Plain. This is consistent with the spatial features observed in Figure 7.

In contrast, stations within unit 33786 have relatively fast Vs30. Unit 33786 is described as an Upper Devonian sedimentary rock unit; geographically it covers regions east of the Lake Erie and parts of the Appalachians. As shown in Figures 7 and 8, TA stations within the Appalachians have distinctively faster Vs30 than the rest of stations in the contiguous US. In the GMNA, geological units within the Appalachians are very complex and diverse; therefore, most individual units only contain five or fewer TA stations and are not shown in Figure 11. For instance, unit 33798 is an Ordovician sedimentary rock unit within the Appalachians, right next to unit 33786, as highlighted on the map. It is a smaller unit, and there are only four TA stations within the unit. Three stations have Vs30 greater than 825 m/s and one station has Vs30 of 571 m/s. The distribution of Vs30 for unit 33798 is much faster than units shown in Figure 11, but unit 33798 is not illustrated as a box because it only includes four stations. On the other hand, unit 33786 is a relatively large geological unit in the Appalachians.

Units 106, 139, and 242 are worth noting in terms of their compact distributions and very short whiskers on both sides. Their compact distributions suggest stations within these units have very similar Vs30 results. In general, nearby stations within the same geological units should have similar subsurface layers, and stations with similar subsurface layers should share similar Vs30. These three geological units fit this ideal assumption; however, high spatial variability of Vs30 cannot be overlooked which makes on-site estimates of Vs30 important.

Comparisons between surficial sediment maps and contiguous stations' Vs30 results show promising trends that fit one's intuitive understanding on relationship between sediment depths and Vs30. In general, one cannot expect large-scale geological features to closely match with near-surface elastic structures because sedimentary thickness can vary on a local scale. Large-scale maps are not built for resolving local features, and near-surface structures are highly variable over a short distance both horizontally and vertically. Although comparisons with large-scale geological units are not ideal and cannot be truly indicative of the local information, we use such comparisons in this section due to the lack of other precise on-site measurements to compare with.

5.3. Comparison With Half-Space Results

In our previous study (Wang & Tanimoto, 2020), we estimated half-space shear-modulus and Vs at 0.02 Hz using the same dataset. In that study, we analyzed data yearly to better examine temporal variation. Although half-space results cannot be used to provide Vs30 values, distributions of peak kernel depths (Figure 4) at various frequencies suggest that half-space results can provide insights on near-surface structures. Half-space results at different frequencies should correlate with Vs30 estimates with various gradients.

Figure 12 shows scatter plots between estimated Vs30 and half-space Vs calculated using Equations 1 and 2. Data from 0.01 to 0.02 Hz are generally more sensitive to deeper structure. If we assume layers at greater depths tend to have faster Vs, half-space results from 0.01 to 0.02 Hz should provide faster Vs than Vs from higher frequencies. We can confirm this trend by looking at distributions in Figure 12. Half-space Vs at lower frequencies (three top panels) tend to be faster than Vs30, whereas half-space Vs at higher frequencies (three bottom panels) tend to be slower than Vs30.

One important pattern illustrated in Figure 12 is the correlation between half-space results and Vs30 from inversion. This correlation is not surprising for two reasons: first, the two methods are closely related. The inversion aims to fit data at discrete frequencies for which the data are proportional to half-space elastic parameters. Second, the half-space Vs is indicative of structure in the near-surface layers, which are the same layers in the inversion results. Although near-surface structure information obtained from the inversion is preferred due to its ability to provide depth-dependent elastic parameters, the strong correlation in Figure 12 shows that the half-space approach provides a first order estimate of Vs in the uppermost layers.

5.4. Frequency Range

While we observe high coherence between seismic and pressure data at 0.05 Hz (Tanimoto & Wang, 2018), there is a greater uncertainty. Therefore, in our inversion we consider two scenarios at every station — set the maximum frequency at either 0.04 or 0.05 Hz. In our final analysis, we select the upper limit at each station by examining inverted models and fits to the data.

In Figure 13, we observe highly correlated Vs30 for the two frequency ranges which suggests inclusion of data from 0.04 to 0.05 Hz has very little effect on the Vs30 estimates. As shown in Figure 4, peak depths of kernels at 0.045 and 0.05 Hz for 355A are very close to the peak depth of the kernel at 0.04 Hz. Although kernels vary among stations, this pattern generally holds which imply data between 0.04 and 0.05 Hz provide depth constraints similar to that of 0.04 Hz.

As an extension of discussion on the upper frequency limit of inversion, we compile distributions of peak depths of shear-modulus sensitivity kernels at all stations. For example, peak depths of 355A and I05D are illustrated as horizontal dashed lines in Figure 4. Figure 14 illustrates the ensemble of peak depths at different frequencies between 0.01 and 0.05 Hz for all stations. The striking feature is that the median peak depths is nearly constant for frequencies greater than 0.03 Hz. This suggests that the depth resolution of frequencies ranging from 0.03 to 0.05 Hz are quite similar.

One caveat about peak depths of sensitivity kernels is that kernels are closely related to pressure-wave speed, c, as reflected in Equation 5. Pressure-wave speeds are the speed of propagating pressure waves at the surface. They are typically within 1–10 m/s. At an individual station, if the pressure-wave speeds are particularly fast or slow, the peak depths of kernels at this station will be different from other stations; therefore, we focus the discussion

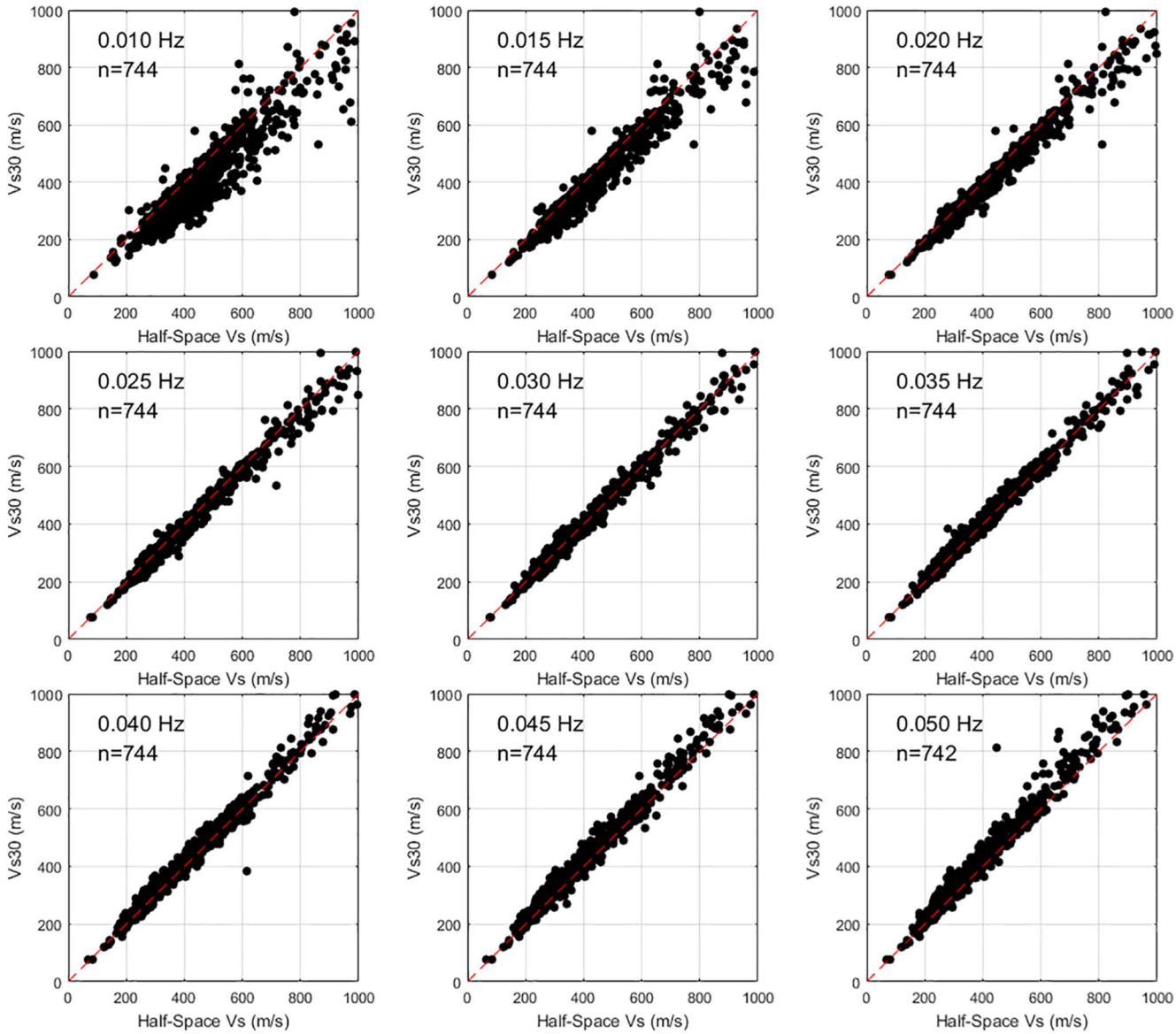

Figure 12. Comparison between half-space Vs (x-axis) and layered Vs30 at various frequencies (y-axis). Limits of all axes are set to 1,000 m/s. Red diagonal dashed lines are one-to-one line. "n" is the total number of points in each panel.

on the general distributions of peak depths across frequencies, instead of focusing on individual stations. Despite the dependency on pressure-wave speeds, distributions of peak depths across different frequencies shown in Figure 14 illustrate the trend in the depth resolution of our results. Namely, the resolved structures become shallower for frequencies from 0.01 to 0.03 Hz and remain relatively constant at a fixed depth from 0.03 to 0.05 Hz.

Figure 14 reveals two limitations of the inversion method. First, our inverted velocity profiles are much smoother compared to other higher-frequency or dense-array methods. Our velocity profiles cannot recover sharp velocity changes. This is evident in the velocity profiles in Figure 3. Because of the low frequency range of our study, the depth resolution is limited. On the other hand, because we aim to estimate Vs30, which is an averaged quantity for the upper 30 m, the inversion method still provides reasonable estimates. Comparison with on-site measured Vs30 in Tanimoto and Wang (2020) supports such a claim. Second, even with the upper frequency limit of 0.05 Hz, we cannot resolve the uppermost layer shallower than 5–10 m. In Figure 14, the minimum median peak depths of shear-modulus kernels are still deeper than 10 m. This suggests we typically lack sensitivity for structures shallower than 10 m. Uppermost velocity profiles of 355A and I05D (Figure 3) show faster Vs at 0–10 m

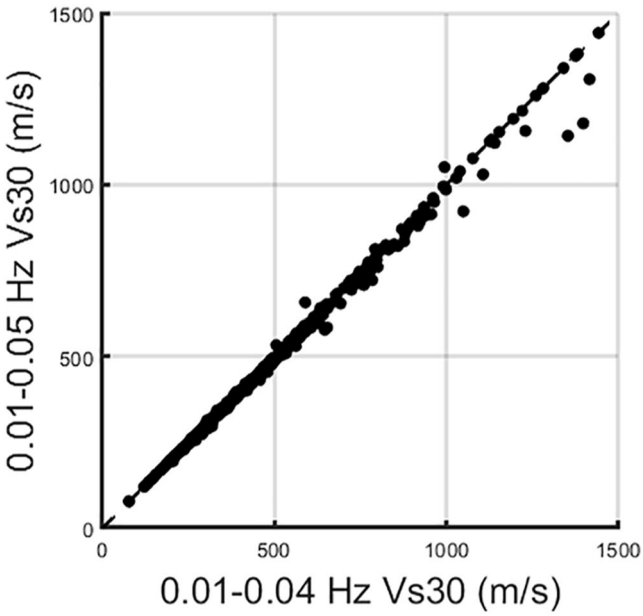

Figure 13. Comparison of inverted Vs30 in two frequency ranges: 0.01–0.05 Hz versus 0.01–0.04 Hz.

than Vs at 10–20 m due to the lack of resolution in uppermost 10 m. The uppermost velocities are essentially aligned with half-space parameters at the highest frequency in the starting models and are not affected by the iterative process due to the lack of sensitivity. To construct more accurate velocity profiles, we need to either extend to higher frequencies or combine with a different approach.

6. Conclusion

In this study, we applied the inversion method (Tanimoto & Wang, 2019) to all available USArray TA stations operating between 1 January 2012 and 1 January 2019. We estimated near-surface elastic parameters for layered structures and Vs30 at these stations. We compared our Vs30 results with various surficial geological maps. There are promising agreements between Vs30 and Quaternary sediment depths. We examine the nature of the inversion method by comparing with half-space results and observing peak depths of sensitivity kernels across frequencies.

We find good correlation between Vs30 and half-space Vs at discrete frequencies between 0.01 and 0.05 Hz. While the inversion method should be used to retrieve important parameters such as Vs30, the half-space approach is much easier to implement and much faster to compute. The half-space approach can be used as a quick tool to determine key information regarding the near-surface structure.

Analysis and examination of peak depths of sensitivity kernels at various frequencies reveal two limitations of the inversion method. First, our estimated velocity profiles are much smoother than those found by conventional high-frequency approaches (e.g., MASW). The limitation is partially resolved because Vs30 is an averaged quantity; the lack of sharp velocity is not critical. Second, the inversion method currently cannot resolve structure shallower than 5 or 10 m given the upper frequency limit of 0.05 Hz. This limitation could potentially introduce errors in our estimations of Vs30 if there are significantly different materials within the uppermost 10 m. We can resolve this limitation by extending our analysis to higher frequencies or by adding new constraints and information to our velocity models.

In conclusion, we estimate Vs30 at 744 TA stations following the inversion method in Tanimoto and Wang (2019). Vs30 is the time-averaged shear-wave velocity down to 30-m depth. It is one of the most important parameters for seismic hazard studies (e.g., Dobry et al., 2000). On a map of the United States, two groups of TA stations stand out. Stations in the Appalachian region tend to have faster Vs30; stations in the Mississippi Alluvial Plain tend to have slower Vs30. These two patterns are consistent with large-scale geological settings and are corroborated by the GMNA (Garrity & Soller, 2009). There are also good agreements between our estimated Vs30 and Quaternary sediment depths in surficial geology maps (Soller et al., 2012; Soller & Garrity, 2018), where stations with thicker underlying sediments tend to have slower Vs30; stations with thin underlying sediments tend to have wider distributions of Vs30. Different distributions of Vs30 on different categories of surficial materials also agree with the general understanding between seismic velocity and sediment types. Although there are no available measured velocity profiles to compare with the TA stations, we previously validated our single-station approach by comparing with measured velocity profile in the Piñon Flat Observatory (Tanimoto & Wang, 2020). We support the more straightforward half-space approach because it correlates well with Vs30 found in the layered structure. The inversion method is still preferred due to its ability to provide depth constraints and to construct layered models.

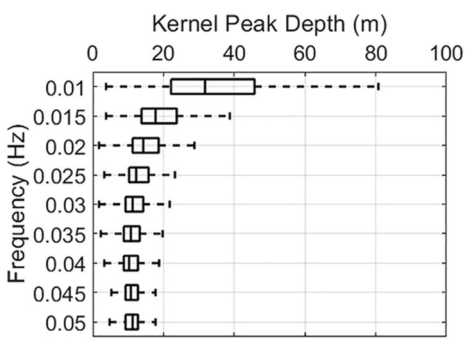

Figure 14. Box plot of peak depths of shear-modulus sensitivity kernels from 0.01 to 0.05 Hz. Vertical line within each box is the median peak depth of that frequency. Boundaries of each box represent 25th and 75th percentile of the distribution. Whiskers extending to each side represent ±2.7σ. Outliers outside of whiskers are omitted.

Data Availability Statement

Data for all results presented in this manuscript are publicly available and accessed from the IRIS DMC (Incorporated Research Institutions for Seismology Data Management Center). Specifically, all TA station information and data can be accessed on http://ds.iris.edu/mda/TA/. For further instruction on downloading data from IRIS, please visit http://ds.iris.edu/ds/nodes/dmc/data/. Codes and output files for this manuscript are available on http://doi.org/10.5281/zenodo.5609870.

Acknowledgments
The authors greatly appreciate Ralph Archuleta for detailed comments and suggestions on the manuscript. The authors also thank Dr. Yannik Behr and other anonymous reviewers for their constructive suggestions, as well as Dr. Douglas Schmitt and Dr. A.-A. Gabriel for their excellent editorial comments. We are grateful for efficient service and great datasets provided by IRIS and the EarthScope project. This work is supported by grants from the United States Geological Survey (USGS #G20AP00024) and the Southern California Earthquake Center (SCEC #19037, #20072). SCEC is funded by NSF Cooperative Agreement EAR-1600087 & USGS Cooperative Agreement G17AC00047.

References

Beauduin, R., Lognonné, P., Montagner, J. P., Cacho, S., Karczewski, J. F., & Morand, M. (1996). The effects of atmospheric pressure changes on seismic signals or how to improve the quality of a station. *Bulletin of the Seismology Society of America*, *86*, 1760–1769. https://doi.org/10.1785/BSSA0860061760

Boore, D. M. (2004). Estimating $\bar{V}_s(30)$ (or NEHRP site classes) from shallow velocity models (depths < 30 m). *Bulletin of the Seismological Society of America*, *94*(2), 591–597. https://doi.org/10.1785/0120030105

Boore, D. M. (2016). Determining generic velocity and density models for crustal amplification calculations, with an update of the Boore and Joyner (1997) generic site amplification for graphic site amplification. *Bulletin of the Seismological Society of America*, *106*(1), 313–317. https://doi.org/10.1785/0120150229

Borcherdt, R. D. (1994). Estimates of site-dependent response spectra for design (methodology and justification). *Earthquake Spectra*, *10*(4), 617–653. https://doi.org/10.1193/1.1585791

Crawford, W. C., Webb, S. C., & Hildebrand, J. A. (1991). Seafloor compliance observed by long-period pressure and displacement measurements. *Journal of Geophysical Research*, *96*(B10), 16151–16160. https://doi.org/10.1029/91jb01577

Dobry, R., Borcherdt, R. D., Crouse, C. B., Idriss, I. M., Joyner, W. B., Martin, G. R., et al. (2000). New site coefficients and site classification system used in recent building seismic code provisions. *Earthquake Spectra*, *16*(1), 41–67. https://doi.org/10.1193/1.1586082

Dou, S., Lindsey, N., Wagner, A. M., Daley, T. M., Freifeld, B., Robertson, M., et al. (2017). Distributed acoustic sensing for seismic monitoring of the near surface: A traffic-noise interferometry case study. *Scientific Reports*, *7*, 11620. https://doi.org/10.1038/s41598-017-11986-4

Garrity, C. P., & Soller, D. R. (2009). Database of the geologic map of North America – Adapted from the map by J. C. Reed, Jr. and others (2005) (Vol. *424*). *U.S. Geological Survey Data Series*. https://doi.org/10.3133/ds424

Kenda, B., Lognonne, P., Spiga, A., Kawamura, T., Kedar, S., Banerdt, W. B., et al. (2017). Modeling of ground deformation and shallow surface waves generated by Martian dust devils and perspectives for near-surface structure inversion. *Space Science Reviews*, *211*, 501–524. https://doi.org/10.1007/s11214-017-0378-0

McNamara, D. E., & Buland, R. P. (2004). Ambient noise levels in the continental United States. *Bulletin of the Seismological Society of America*, *94*(4), 1517–1527. https://doi.org/10.1785/012003001

Müller, T., & Zürn, W. (1983). Observation of gravity changes during the passage of cold fronts. *Journal of Geophysics*, *53*, 155–162.

Nakamura, Y. (1989). A method for dynamic characteristics estimation of subsurface using microtremor on the ground surface. *Quarterly Report of Railway Technical Research*, *30*, 25–33.

Park, B. C., Miller, D. R., & Xia, J. (1999). Multichannel analysis of surface waves. *Geophysics*, *64*(3), 659–808. https://doi.org/10.1190/1.1444590

Park, S., & Elrick, S. (1998). Predictions of shear-wave velocities in southern California using surface geology. *Bulletin of the Seismological Society of America*, *88*(3), 677–685. https://doi.org/10.1785/bssa0880030677

Park, S., & Ishii, M. (2018). Near-surface compressional and shear wave speeds constrained by body-wave polarization analysis. *Geophysical Journal International*, *213*(3), 1559–1571. https://doi.org/10.1093/gji/ggy072

Raspet, R., Hickey, C. J., & Bipin, K. (2022). Corrected tilt calculation for atmospheric pressure-induced seismic noise. *Applied Sciences*, *12*(3), 1247. https://doi.org/10.3390/app12031247

Rodgers, P. W. (1968). The response of the horizontal pendulum seismometer to Rayleigh and love waves, tilt, and free oscillations of the Earth. *Bulletin of the Seismological Society of America*, *58*(5), 1385–1406. https://doi.org/10.1785/bssa0580051385

Sánchez-Sesma, F. J., & Crouse, C. B. (2015). Effects of site geology on seismic ground motion: Early history. *Earthquake Engineering & Structural Dynamics*, *44*, 1099–1113. https://doi.org/10.1002/eqe.2503

Soller, D. R., & Garrity, C. P. (2018). Quaternary sediment thickness and bedrock topography of the glaciated United States east of the Rocky Mountains. *U.S. Geological Survey Scientific Investigations Map*, *3392*. https://doi.org/10.3133/sim3392

Soller, D. R., Reheis, M. C., Garrity, C. P., & Van Sistine, D. R. (2012). Map database for surficial materials in the conterminous United States. *U.S. Geological Survey Data Series*, *425*. https://doi.org/10.3133/ds425

Sorrells, G. G. (1971). A preliminary investigation into the relationship between long-period seismic noise and local fluctuations in the atmospheric pressure field. *Geophysical Journal International*, *26*(1–4), 71–82. https://doi.org/10.1111/j.1365-246X.1971.tb03383.x

Sorrells, G. G., McDonald, J. A., Der, Z. A., & Herrin, E. (1971). Earth motion caused by local atmospheric pressure changes. *Geophysical Journal International*, *26*(1–4), 83–98. https://doi.org/10.1111/j.1365-246X.1971.tb03384.x

Tanimoto, T., & Li, Y. (2020). Nature of low-frequency, atmosphere-generated seismic noise. *Journal of Geophysical Research: Solid Earth*, *125*, 7, https://doi.org/10.1029/2020JB019423

Tanimoto, T., & Rivera, L. (2008). The ZH ratio method for long-period seismic data: Sensitivity kernels and observational techniques. *Geophysical Journal International*, *172*(1), 187–198. https://doi.org/10.1111/j.1365-246X.2007.03609.x

Tanimoto, T., & Wang, J. (2018). Low-frequency seismic noise characteristics from the analysis of co-located seismic and pressure data. *Journal of Geophysical Research: Solid Earth*, *123*(7), 5853–5885. https://doi.org/10.1029/2018JB015519

Tanimoto, T., & Wang, J. (2019). Theory for deriving shallow elasticity structure from co-located seismic and pressure data. *Journal of Geophysical Research: Solid Earth*, *124*(6), 5811–5835. https://doi.org/10.1029/2018JB017132

Tanimoto, T., & Wang, J. (2020). Shallow elasticity structure from colocated pressure and seismic stations in the Piñon Flat Observatory and estimation of Vs30. *Geophysical Journal International*, *222*(1), 678–696. https://doi.org/10.1093/gji/ggaa195

Tanimoto, T., & Wang, J. (2021). Incorporating wind information in the inversion of co-located pressure and seismic data for shallow elastic structure. *Journal of Geophysical Research: Solid Earth*, *126*(5). https://doi.org/10.1029/2020JB021162

Tarantola, A. (2005). Inverse problem theory and methods for model parameter estimation, statistical modeling and decision science. *SIAM*. https://doi.org/10.1137/1.9780898717921

Thompson, E., & Silva, W. (2013). *Empirical assessment of site amplification and development of NEHRP factors for CEUS: Collaborative research with Pacific Engineering and Tufts University*. U.S. Geological Survey. (Final Technical Report) Retrieved from https://earthquake.usgs.gov/cfusion/external_grants/reports/G12AP20004.pdf

Trifunac, M. D. (2016). Site conditions and earthquake ground motion – A review. *Soil Dynamics and Earthquake Engineering*, *90*, 88–100. https://doi.org/10.1016/j.soildyn.2016.08.003

Tytell, J., Vernon, F., Hedlin, M., De Groot Hedlin, C., Reyes, J., Busby, B., et al. (2016). The US array transportable array as a platform for weather observation and research. *Bulletin of the American Meteorological Society*, *97*, 603–619. https://doi.org/10.1175/bams-d-14-00204.1

Wald, D., & Allen, T. (2007). Topographic slope as a proxy for seismic site conditions and amplification. *Bulletin of the Seismological Society of America*, *97*(5), 1379–1395. https://doi.org/10.1785/0120060267

Wang, J., & Tanimoto, T. (2020). Estimating near-surface rigidity from low-frequency noise using collocated pressure and horizontal seismic data. *Bulletin of the Seismological Society of America*, *110*(4), 1960–1970. https://doi.org/10.1785/0120200098

Wilcox, R. (2012). Estimating measures of location and scale, Chapter 3: Introduction to robust estimation and hypothesis testing. In R.Wilcox, *Statistical modeling and decision science* (3rd ed., pp. 43–101). Academic Press. https://doi.org/10.1016/b978-0-12-386983-8.00003-2

Will, C. J., Gutierrez, C. I., Perez, F. G., & Branum, D. M. (2015). A next generation VS_{30} map for California based on geology and topography. *Bulletin of the Seismological Society of America*, *105*(6), 3083–3091. https://doi.org/10.1785/0120150105

Wills, C. J., Petersen, M., Bryant, W. A., Reichle, M., Saucedo, G. J., Tan, S., et al. (2000). A site-conditions map for California based on geology and shear-wave velocity. *Bulletin of the Seismological Society of America*, *90*(6B), S187–S208. https://doi.org/10.1785/0120000503

Yong, A., Martin, A., Stokoe, K., & Diehl, J. (2013). ARRA-funded V_{S30} measurements using multi-technique approach at strong-motion stations in California and Central-Eastern United States (Open-File Rept.). *U.S. Geological Survey*, *2013–1102*, 60. http://pubs.usgs.gov/of/2013/1102/